PROCEEDINGS A

royalsocietypublishing.org/journal/rspa

Research

Cite this article: Veney J, D'Souza K. 2023 Frequency tunable electromagnetic vibration energy harvester using piecewise linear nonlinearity. *Proc. R. Soc. A* **479**: 20230207. https://doi.org/10.1098/rspa.2023.0207

Received: 27 March 2023
Accepted: 22 August 2023

Subject Areas:
mechanical engineering, energy

Keywords:
energy harvester, piecewise linear, nonlinear dynamics

Author for correspondence:
Kiran D'Souza
e-mail: dsouza.60@osu.edu

Frequency tunable electromagnetic vibration energy harvester using piecewise linear nonlinearity

Jacob Veney and Kiran D'Souza

Department of Mechanical and Aerospace Engineering, The Ohio State University, 2300 W Case Road, Columbus, OH 43235, USA

JV, 0000-0002-4507-9379

Vibration energy harvesting is increasingly being seen as a viable energy source to provide for our energy-dependent society. There has been great interest in scavenging previously unused or wasted energy in a large variety of systems including vibrating machinery, ocean waves and human motion. In this work, a bench-top system of a piecewise-linear nonlinear vibration energy harvester is studied. A similar idealized model of the system had previously been studied numerically, and in this work the method is adjusted to better account for the physical system. This new design is able to actively tune the system's resonant frequency to match the current excitation through the adjustment of the gap size between the oscillator and mechanical stopper; thus maximizing the system response over a broad frequency range. This design shows an increased effective frequency bandwidth compared with traditional linear systems and improves upon current nonlinear designs that are less effective than linear harvesters at resonance. In this paper, the physical system is tested at various excitation conditions and gap sizes to showcase the new harvester design's effectiveness.

1. Introduction

As society continues to move towards a digital and electrified future, there is an increasing need to find new or improved renewable energy methods to meet the unprecedented demand, while also reducing dependency on carbon-based fuel sources. One promising

THE ROYAL SOCIETY PUBLISHING

renewable energy source comes from vibration energy harvesters. These devices operate by scavenging the energy in ambient vibrations and converting it to usable electrical power [1,2]. With many possible applications, this technology has been of great interest to researchers recently. In engineered systems such as rotating machinery or bridges, a vibration energy harvester (VEH) could be used to scavenge the wasted energy in vibrations [3–5]. The previously unused energy could then be used to power a suite of sensors monitoring the system conditions. This is especially useful in applications where external wiring or the use of batteries is unfeasible. VEHs could also be used for much larger electrical grid-scale applications by extracting energy from the ocean waves in coastal waters [6,7]. In the USA alone, it is estimated that there is as much as 2.64 trillion kWh of energy potential in these coastal waters [8]. This is about 64% of the yearly utility-scale energy production in the country. By tapping into this relatively unused renewable energy source, dramatic increases in clean energy production and decreases in fossil fuel reliance are possible [9].

The most simple VEHs operate by exploiting the motion of a simple lightly damped linear oscillator at resonance [10]. When the dominant frequency of the ambient vibration matches the system's resonant frequency, the motion of the oscillator is greatly amplified compared with the ambient vibrations. The motion of the oscillator is then used to generate electricity through a variety of methods (electromagnetic, piezoelectric, etc.). The issue with this simple design lies in its inherent frequency response characteristics. While at resonance the performance is optimal, as the ambient vibration strays from resonance, the performance of this simple device dramatically decreases. This is not ideal for many applications where the ambient frequency is often changing, leading to suboptimal performance. To increase the efficiency of VEH designs and broaden the effective frequency range, researchers have devised alternative methods of energy harvesting. One alternative method is to use a nonlinear vibration energy harvester [11–18]. These designs leverage nonlinearities in the materials or geometry to broaden the effective frequency range of the VEH. While these methods did show an increased frequency range, the maximum performance at resonance is reduced compared with linear harvesters at resonance. Another alternative method used is array harvesting. In these systems, a large number of linear VEHs with varying resonant frequencies are combined, to try to ensure that the device is operating near at least one of the resonant values. While one of the harvesters can match the performance of a linear VEH at resonance, the energy density is reduced due to the increased system complexity making these systems suboptimal in practical applications [19–21].

Another promising method of broadband vibration energy harvesting of interest to researchers is bi-stable or multi-stable systems that can leverage the largest amplitude response to ensure maximum performance of the system. Wang *et al.* [22,23] proposed a bistable harvester with a rolling central magnet. Using the forces of the opposing magnets in the system, an oscillator is created that is used to harvest ambient vibrations. As is common with many of these systems, this system did not show high vibration performance for all excitation conditions, namely the reverse frequency sweep. Bendame *et al.* [24,25] also proposed a springless VEH with stoppers positioned at the ends of the harvester. In this system, a nonlinearity in the form of a mechanical stopper is introduced into the traditional linear system creating a piecewise-linear (PWL) nonlinear oscillator to change the dynamics of the system. While increased bandwidth was shown in this system, the harvester still did not perform as effectively as a tuned linear harvester at resonance for individual frequency points. These proposed PWL harvesters have taken many forms [26–33], but the maximum performance compared with a linear system at resonance is still reduced.

In order to overcome these obstacles to effective energy harvesting, a new PWL nonlinear harvester has recently been proposed and numerically investigated [34]. In the proposed design, an actively controlled mechanical stopper is positioned across from the traditional linear VEH. By adjusting the position of the stopper, the resonant frequency of the system can then be tuned, ensuring optimal performance even when the excitation varies. Unlike other methods using PWL systems, this proposed method is able also to match the theoretical performance of a linear harvester at a resonance frequency within its range of operation. To calculate the optimal gap size, the bilinear amplitude approximation (BAA) method is used [35]. This is a method previously developed to efficiently predict the response of complex PWL nonlinear systems, and has been

demonstrated both computationally and experimentally [36–39]. The BAA method is used before operation of the device to precompute the resonant gap sizes over the frequency range of interest. While the device is operating, the amplitude and frequency of the excitation signal are extracted. Using the precomputed resonant gap sizes and the extracted signal information, the gap is then set to the optimal position. This process is then repeated during the operation of the device. The previous computational study showed that this design performs more effectively than many other VEHs for a number of cases since it can operate efficiently for a wide variety of excitation conditions [34].

In this work, an experimental investigation of the new harvester design is conducted. In order to demonstrate the effectiveness of the new PWL nonlinear harvester, the system is tested at a variety of excitation conditions and the dynamics of the system are monitored. These results are then compared with the computational predictions. Modifications were made to the previous idealized computational model presented in [34] to account for parameters not considered in the previous idealized study. The remainder of this work is organized as follows. First, the computational methodology section introduces the changes to the computational model. The dynamics of the system, control process and electromagnetic model are also introduced in this section. Next, the experimental set-up and parameter identification process are presented in the experimental methodology section. Finally, the physical study section tests the system at various excitations and gap sizes to prove the efficacy of the design.

2. Computational methodology

This section outlines the new mathematical model of the PWL harvester that includes the contact mass, the solution method using BAA with the additional contact mass and the model of the electromagnetic induction that will predict the power output of the harvester.

(a) Mechanical mathematical model

The mechanical model for the system is shown below in figure 1. As mentioned, the previous computational study did not account for the contact mass of the stopper. Changes were made to the computational process to model the physical system more accurately and are introduced below.

In the harvester design, a simple linear oscillator of mass m, stiffness k and damping coefficient c is positioned across from a linear actuator. Attached to the linear actuator is a mechanical stopper of mass m^*, stiffness k^* and damping c^*. It is assumed that the damping in both components is linear and viscous. These two components are intermittently contacting as the system is excited from the base by displacement $y(t)$. The linear actuator is used to set the gap size $g(t)$. Note that the gap size is solely dependent on the actuator position and does not depend on the position of the mass $x(t)$. In order to convert the mechanical energy of the system to electrical energy, a conductor coil is also wound around the axis of motion of the central mass, which is a magnetic material with poles oriented in the direction of motion as seen in figure 1. A change from the computational study is that the mass of the stopper m^* has been included to account for the inertial effects of the stopper.

The equations of motion of the system are shown below in equation (2.1). The variable $\bar{x} = x - y$ is the motion of the mass with respect to the base and the parameter $\bar{m} = m + m^*$ is the combined mass of the oscillator and the contact mass.

$$\left.\begin{aligned} &\bar{m}\ddot{\bar{x}}_c(t) + (c + c^*)\dot{\bar{x}}_c(t) + (k + k^*)\bar{x}_c(t) \\ &\quad = -\bar{m}\ddot{y}(t) + c^*\dot{g}(t) + k^*g(t) \qquad \text{when } \bar{x} \geq g, \\ \text{and} \quad &\bar{m}\ddot{\bar{x}}_o(t) + c\dot{\bar{x}}_o(t) + k\bar{x}_o(t) = -m\ddot{y}(t) \qquad \text{when } \bar{x} < g. \end{aligned}\right\} \tag{2.1}$$

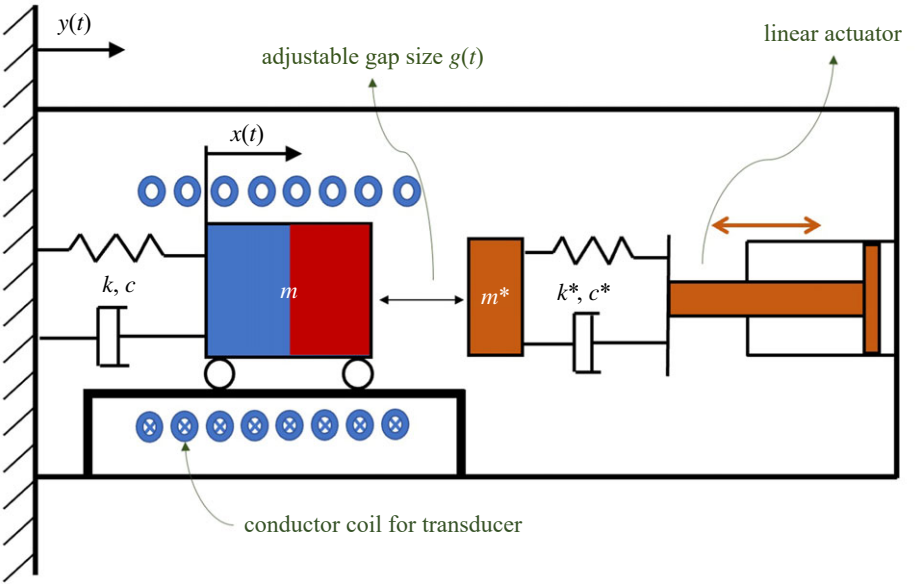

Figure 1. Mechanical model of the PWL harvester with electromagnetic transducer. Design consists of a PWL oscillator with a linear actuator controlling the gap size.

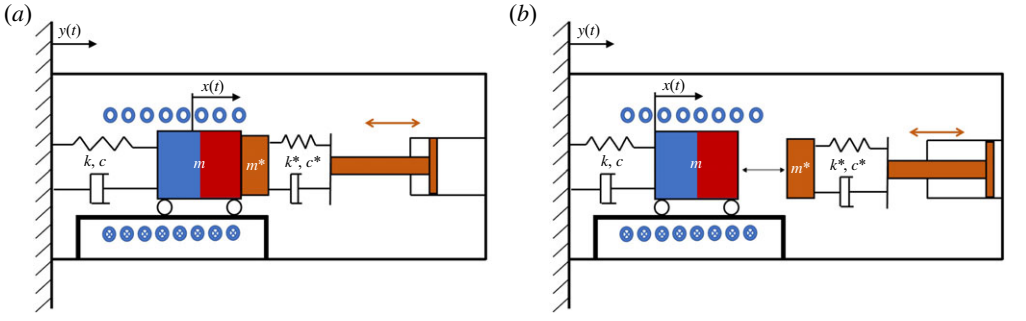

Figure 2. (*a*) System in closed state. (*b*) System in open state.

Note that the subscript c denotes the system operating in the closed/sliding state or $\bar{x} \geq g$ and the subscript o denotes the system in the open state or $\bar{x} < g$. The system in its closed and open states is shown in figure 2.

After dividing by the mass in each equation, the system can be rewritten as

$$\left.\begin{aligned} &\ddot{\bar{x}}_c(t) + 2(\zeta_{c1}\omega_{c1} + \zeta_{c2}\omega_{c2})\dot{\bar{x}}_c(t) + (\omega_{c1}^2 + \omega_{c2}^2)\bar{x}(t) \\ &\quad = \ddot{y}(t) + 2\zeta_{c2}\omega_{c2}\dot{g}(t) + \omega_{c2}^2 g(t) \qquad \text{when } \bar{x} \geq g, \\ \text{and} \quad &\ddot{\bar{x}}_o(t) + 2\zeta_o\omega_o\dot{\bar{x}}_o(t) + \omega_o^2\bar{x}_o(t) = -\ddot{y}(t) \quad \text{when } \bar{x} < g. \end{aligned}\right\} \tag{2.2}$$

The parameters introduced in equation (2.2) are defined below.

$$\omega_o^2 = \frac{k}{m} \quad \text{and} \quad \zeta_o = \frac{c}{2m\omega_o}$$

and

$$\omega_{c1}^2 = \frac{k}{\bar{m}}, \quad \zeta_{c1} = \frac{c}{2\bar{m}\omega_{c1}}, \quad \omega_{c2}^2 = \frac{k^*}{\bar{m}} \quad \text{and} \quad \zeta_{c2} = \frac{c^*}{2\bar{m}\omega_{c2}}.$$

Next, time-related dimensionless variables are introduced and listed below.

$$\tau_o = \omega_o t \quad \text{and} \quad \rho_o = \frac{\alpha}{\omega_o}$$

and

$$\tau_c = \omega_{c1} t, \quad \rho_c = \frac{\alpha}{\omega_{c1}} \quad \text{and} \quad \rho_c^* = \frac{\omega_{c2}}{\omega_{c1}}.$$

For simplicity and due to the fact that BAA was developed for use with periodic excitation, it is assumed the system is subjected to harmonic excitation $y(t) = y_0 \sin(\alpha t)$ where α is the excitation frequency and y_0 is the amplitude of excitation. Equation (2.2) can then be rewritten with the dimensionless variables as:

$$\left.\begin{aligned} &\ddot{\bar{x}}_c(\tau_c) + 2(\zeta_{c1} + \zeta_{c2}\rho_c^*)\dot{\bar{x}}_c(\tau_c) + (1 + \rho_c^{*2})\bar{x}(\tau_c) \\ &\quad = \rho_c^2 y_0 \sin(\rho_c \tau_c) + 2\zeta_{c2}\rho_c^* \dot{g}(\tau_c) + \rho_c^{*2} g(\tau_c) \quad \text{when } \bar{x} \geq g \\ \text{and} \quad &\ddot{\bar{x}}_o(\tau_o) + 2\zeta_o \dot{\bar{x}}_o(\tau_o) + \bar{x}_o(\tau_o) = \rho_o^2 y_0 \sin(\rho_o \tau_o) \quad \text{when } \bar{x} < g. \end{aligned}\right\} \tag{2.3}$$

Note that for a certain excitation frequency α, $\tau_o \neq \tau_c$ and $\rho_o \neq \rho_c$. This is due to the dimensionless variables chosen above. The following equation gives the conversions between the closed and open domains:

$$\tau_o = \tau_c \sqrt{\frac{\bar{m}}{m}} \quad \text{and} \quad \rho_o = \rho_c \sqrt{\frac{m}{\bar{m}}}. \tag{2.4}$$

Finally, to allow for precomputation of the system response independent of the base motion, the following displacement-related dimensionless variables are introduced as

$$u = \frac{\bar{x}}{y_0} \quad \text{and} \quad \delta = \frac{g}{y_0}. \tag{2.5}$$

By scaling $\bar{x}$ and g by the base amplitude y_0, the results of the computational process can be applied to any level of base excitation, enabling offline precomputation. The final equations of motion of the system are then given in equation (2.6) as

$$\left.\begin{aligned} &\ddot{u}_c(\tau_c) + 2(\zeta_{c1} + \zeta_{c2}\rho_c^*)\dot{u}_c(\tau_c) + (1 + \rho_c^{*2})u(\tau_c) \\ &\quad = \rho_c^2 \sin(\rho_c \tau_c) + 2\zeta_{c2}\rho_c^* \dot{\delta}(\tau_c) + \rho_c^{*2}\delta(\tau_c) \quad \text{when } u \geq \delta, \\ \text{and} \quad &\ddot{u}_o(\tau_o) + 2\zeta_o \dot{u}_o(\tau_o) + u_o(\tau_o) = \rho_o^2 \sin(\rho_o \tau_o) \quad \text{when } u < \delta. \end{aligned}\right\} \tag{2.6}$$

(b) System dynamics

The BAA method is used to solve equation (2.6) and predict the system response for various gap sizes. The fundamental idea of the method is that the vibration cycle of a PWL oscillator is simply the coupled response of the system in its open and closed states. It is also assumed that for the single vibration cycle, the response is only in each state once, giving an overall period of $T = T_o + T_c$; T_o being the time interval in the open state and T_c being the time interval in the closed state. The coordinates of the system in the open and closed states can then be given by the following equation by combining the linear steady-state and transient responses as:

$$\left.\begin{aligned} u_c(\tau_c) &= e^{-\bar{\zeta}\bar{\rho}\tau_c} a_c \sin\left(\sqrt{1-\bar{\zeta}^2}\bar{\rho}\tau_c + \phi_c\right) \\ &\quad + \frac{(\rho_c/\bar{\rho})^2 \sin(\rho_c \tau_c - \theta_c + \Psi)}{\sqrt{[1-(\rho_c/\bar{\rho})^2]^2 + (2\bar{\zeta}\rho_c/\bar{\rho})^2}} + \delta\left(\frac{\rho_c^{*2}}{1+\rho_c^{*2}}\right), \\ \text{and} \quad u_o(\tau_o) &= e^{-\zeta_o \tau_o} a_o \sin\left(\sqrt{1-\zeta_o^2}\tau_o + \phi_o\right) \\ &\quad + \frac{\rho_o^2 \sin(\rho_o \tau_o - \theta_o + \Psi)}{\sqrt{(1-\rho_o^2)^2 + (2\zeta_o \rho_o)^2}}, \end{aligned}\right\} \tag{2.7}$$

where $\bar{\zeta} = (\zeta_{c1} + \zeta_{c2}\rho_c^*)/\sqrt{1+\rho_c^{*2}}$, $\bar{\rho} = \sqrt{1+\rho_c^{*2}}$, $\theta_o = \tan^{-1}(2\zeta_o\rho_o/(1-\rho_o^2))$ and $\theta_c = \tan^{-1}(2\bar{\zeta}\rho_c\bar{\rho}/(\bar{\rho}^2+\rho_c^2))$. Other variables introduced include scalar coefficients representing the transient response amplitude a_c and a_o, phase angles of the transient response ϕ_c and ϕ_o, and the phase difference between the excitation and steady-state response resulting from the PWL nonlinearity Ψ. A nonlinear optimization solver is then used to minimize the residual of the compatibility conditions given in equation (2.8).

$$\left.\begin{aligned} u_c(0) &= \delta, \\ u_c(T_c) &= \delta, \\ u_o(T_c) &= \delta, \\ u_o(T_c + T_o) &= \delta, \\ \dot{u}_c(T_c) &= \dot{u}_o(T_c) \\ \text{and} \quad \dot{u}_c(0) &= \dot{u}_o(T_c + T_o). \end{aligned}\right\} \tag{2.8}$$

Note that T_c is an additional unknown introduced in equation (2.8). All compatibility conditions shown are applied at the transition between states. The first four conditions are the displacement compatibility conditions and the last two represent the velocity compatibility. To solve for the system unknowns, the Matlab function [40] 'lsqnonlin' is used in this computational process. With these values determined, the entire vibration cycle for any gap size can be constructed. For a more detailed explanation of the BAA method, refer to previous works on this topic [34,35].

(c) Control process

In order to effectively maintain high amplitude responses, the control method proposed in the computational study will be used along with the updated modelling approach discussed herein. This will allow for the gap to be adjusted to the optimal position over the bounded frequency range, increasing the PWL oscillator's vibration amplitude. The steps of the control process are given as follows:

(a) The excitation signal is measured over a certain duration T_s.
(b) The dominant frequency α_{est} and amplitude $y_{0,\text{est}}$ of the measured signal are identified using frequency and amplitude estimators.
(c) The resonant gap size δ_r corresponding to the estimated frequency ρ_{est} is found from the precomputed BAA results. (Interpolate neighbouring values if ρ_{est} is not an exact value in the precomputed results.)
(d) To avoid the jump phenomenon, δ_{opt} is set to a fraction of the calculated δ_r. ($\delta_{\text{opt}} = a\delta_r$, where $0 < a < 1$.)
(e) The gap size is re-dimensionalized and adjusted to $g_{\text{opt}} = y_{0,\text{est}} * \delta_{\text{opt}}$.
(f) Steps (a)–(e) are repeated for the duration of operation.

The signal estimation methods in this work were developed by Zhivomirov *et al.* [41] and Lyons [42]. Through discrete Fourier transform techniques, the windowed signal is used to extract the estimated frequency and amplitude. As mentioned previously, the BAA method is effectively leveraged due to the non-dimensionalization used in the calculations. This allows for a computationally efficient calculation of the resonant gap size δ_r since the gap sizes can be precomputed offline in the frequency range of interest. The sole active calculation during the process is the frequency and amplitude extraction. As briefly mentioned above in step (d), the gap size δ_{opt} is calculated by scaling down the precomputed δ_r. This is to avoid the undesired jump phenomenon that was extensively studied in [34]. This phenomenon is also discussed in §4a. A summarized form of the control process used in this work is shown in figure 3.

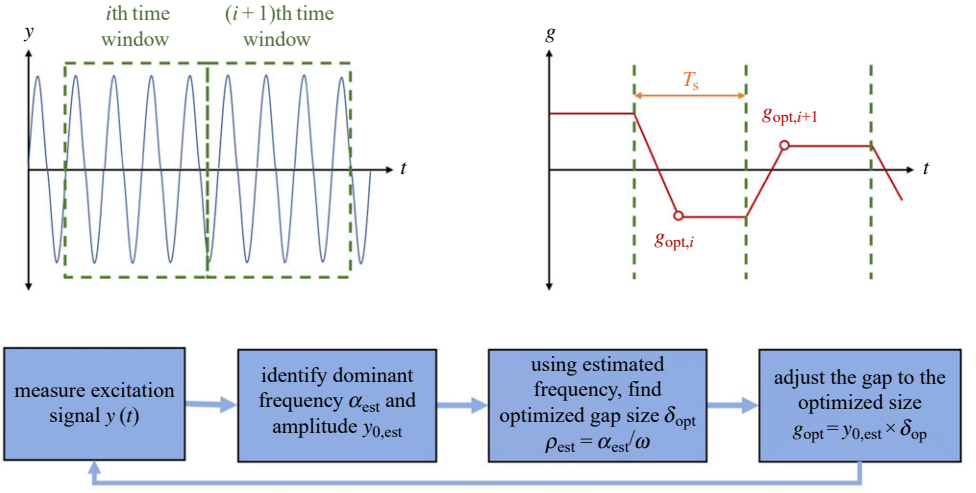

Figure 3. Summarized control process for the PWL system. Note that the gap size in the $(i + 1)$th window is determined by the signal estimation in the ith window.

(d) Electromagnetic induction

As power generation was not considered in the previous study, a computational model of the electromagnetic induction of the harvester was created. For this investigation, an electromagnetic transducer was selected. This is a commonly used method of energy conversion for vibration energy harvesting, especially in large-scale applications including wave power generation [43,44]. The bench-top scale with relatively large vibration amplitudes also led to the selection of an electromagnetic transducer.

In the physical experiment, a magnet is attached to the oscillating mass with a coil mounted around it. According to Faraday's Law, the induced electromotive force (emf) in the coil to the relative motion is given as

$$\text{emf} = -\frac{\mathrm{d}\psi}{\mathrm{d}t} = -\frac{\mathrm{d}\psi}{\mathrm{d}z}\left|\frac{\mathrm{d}z}{\mathrm{d}t}\right|, \tag{2.9}$$

where the total magnetic flux through the coil turns is denoted by ψ. The flux through a single coil [45] can then be represented as

$$\psi = \frac{\mu_0 M}{2}\left[\frac{1}{\sqrt{r^2+z^2}} - \frac{z^2}{(r^2+z^2)^{3/2}}\right]. \tag{2.10}$$

To find the change in flux through a coil of radius r and distance z from the dipole centre, equation (2.10) is differentiated with respect to z giving

$$\frac{\mathrm{d}\psi}{\mathrm{d}z} = \frac{\mu_0 M}{2}\left[\frac{2*z^3}{(r^2+z^2)^{5/2}} - \frac{3z}{(r^2+z^2)^{3/2}}\right], \tag{2.11}$$

where the parameter μ_0 denotes the permeability of free space and M denotes the magnetic moment of the magnet. Finally, the change in magnetic flux through the entire coil of N turns and length l is expressed as

$$\left.\begin{aligned}\frac{\mathrm{d}\psi}{\mathrm{d}z} &= \frac{\mu_0 M}{2}\sum_{n=-N/2}^{n=N/2} z_n\left[\frac{2*z_n^2}{(r^2+z_n^2)^{5/2}} - \frac{3}{(r^2+z_n^2)^{3/2}}\right]\\ \text{where}\quad z_n &= z + n\left(\frac{l}{N-1}\right).\end{aligned}\right\} \tag{2.12}$$

The average power generated by the system is then calculated using the root mean squared voltage v_{rms}^2 and load resistance R values as shown in equation (2.13) as

$$P_{\text{avg}} = \frac{v_{\text{rms}}^2}{R}. \tag{2.13}$$

3. Experimental methodology

In this section, the experimental set-up used for the investigation is introduced and then the process for identifying the necessary system parameters is discussed.

(a) Experimental set-up

The experimental set-up consists of a base-excited mass-spring oscillator intermittently contacting a mechanical stopper. A top down view of the set-up can be seen in figure 4. Mounted onto the central linear guide rail is a carriage that is connected to the base by extension springs. On one side of the guide rail there is a mechanical stopper attached to a linear actuator (P8, Actuonix) positioned collinear to the mass motion. The actuator is used to change the size of the gap between the mass and stopper, therefore tuning the resonant frequency of the system to match the current excitation signal. To simulate the base-excitation motion in the rail direction, an electrodynamic shaker (ET-126B, Labworks) is connected to the testing surface, which is also mounted onto linear guide rails and carriages. Laser displacement sensors (IL-100, Keyence) are also used to measure the system dynamics. The sensor head mounted next to the shaker is used to track the base motion (y) and the sensor mounted onto the vibrating surface is used to track the mass motion relative to the base ($\bar{x}$). In order to control the gap size and collect measurement data, the individual system components are connected to a computer running a Matlab script which actively estimates the signal parameters and sets the gap to the necessary position.

(b) Parameter identification

Before beginning the investigation, experiments were conducted to extract the parameters to create an accurate system model. Through the frequency sweeps with the single degree of freedom systems, the parameters in figure 1 (i.e. m, c and k) can be identified. This is a necessary step in the process because the damping must be experimentally determined and the inertia in the springs cannot be neglected in the physical system.

First, the single DOF system consisting of the mass-spring oscillator was subjected to a sinusoidal frequency up-sweep while the motion of the mass and base were recorded. Using the measured responses, the displacement transmissibility curve of the system shown in figure 5 was constructed. The system was also excited by a frequency down-sweep for frequency response validation purposes. The frequency that exhibited the maximum response gives the resonant frequency of the single DOF system and the damping ratio can be calculated using the half-power bandwidth method given in equation (3.1)

$$\zeta = \frac{f_2 - f_1}{2f_{\text{peak}}}, \tag{3.1}$$

where f_{peak} is the resonant frequency of the system and f_1 and f_2 are the frequencies at the half-power points. The extracted resonant frequency and half-power points for the frequency sweep are also shown in figure 5.

Next, using the resonant frequency and damping ratio, the natural frequency of the system can be calculated. After measuring the mass of the central carriage, the damping c and stiffness k can be determined from the known relations of damped linear oscillators. In the investigation, this process was conducted twice with differing carriage mass values. It was expected that for each case, the stiffness and damping values would be equal and solely the mass value would change; however, in initial testing this was not the case. It was hypothesized that the inertia of the springs

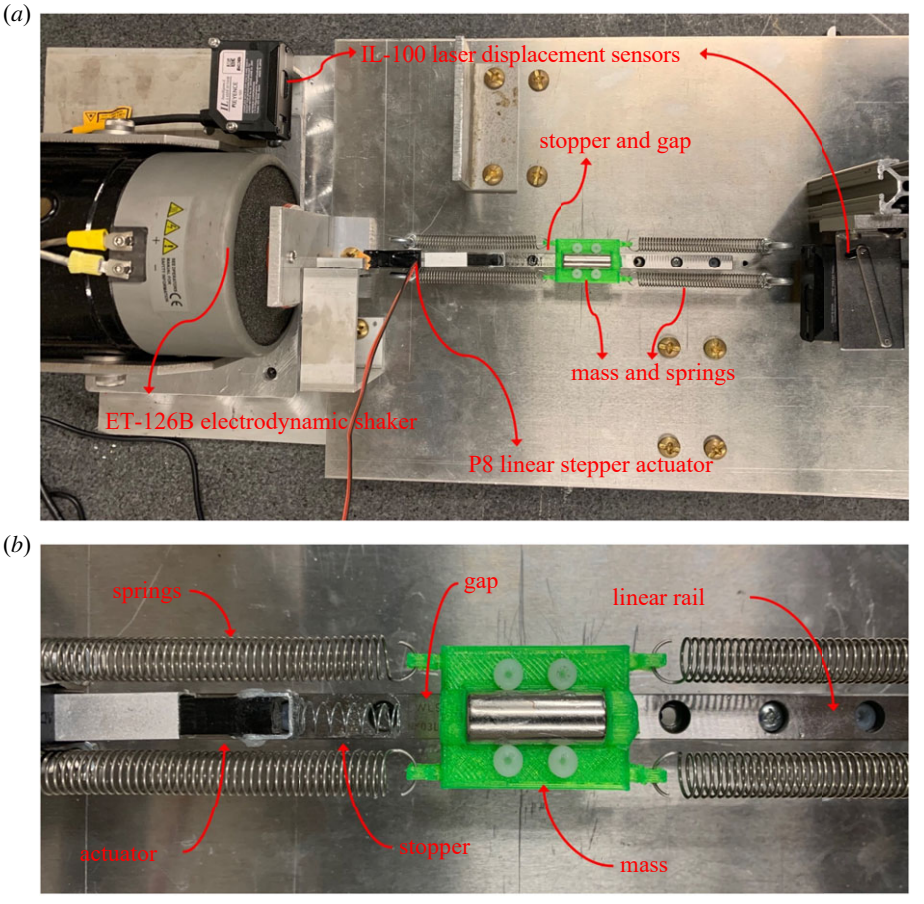

Figure 4. (*a*) Experimental set-up top-view. (*b*) Close-up view of mass and stopper.

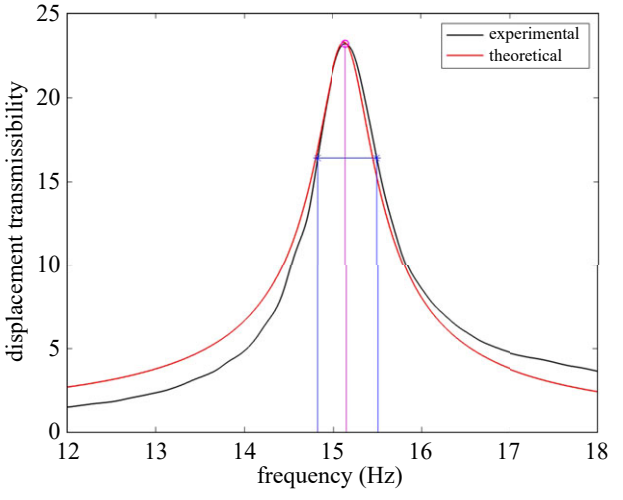

Figure 5. Displacement transmissibility of the 1 DOF system with half power points indicated by blue stars and resonant peak indicated by a magenta circle. The red curve shows the frequency response of a system with the optimized system parameters.

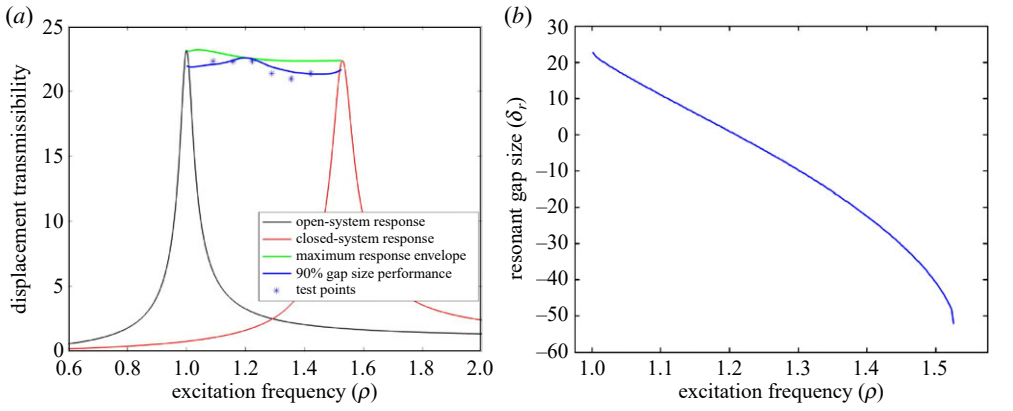

Figure 6. (*a*) Response envelope and linear responses. (*b*) Precomputed optimal gap sizes.

Table 1. Optimized system parameters from system identification.

case	m (g)	k (N m^{-1})	c (N s m^{-1})
1	26.52	346.91	0.1583
2	38.49	348.71	0.1575

was significant and had to be accounted for in order to effectively characterize the system. To account for this additional mass, the following optimization equation was used

$$m_i = m_{\text{nom}} + \frac{4}{3} * m_{\text{spring}} * w_i, \tag{3.2}$$

where m_{nom} is the measured cart mass, m_{spring} is the measured mass of one spring and w_i is a weighting factor between 0 and 2.5. One-third of the spring mass was chosen as a reference value for the mass contribution as this is the effective mass of an ideal spring. The necessary parameters were then calculated for the differing mass contributions and the average value of k and c between the two cases was then chosen for the remainder of the analysis. The case using the lower mass value (i) corresponds to solely the mass of the cart and springs and the case with the higher mass value (ii) corresponds to the same system with the addition of the magnet for optimization purposes. The parameters identified for the nominal system are given in table 1.

As the values of stiffness and damping did not converge to single values, the average values of $k = 347.81\,\text{N m}^{-1}$ and $c = 0.1579\,\text{N s m}^{-1}$ were used as the system parameters for the subsequent analysis. The same process was then conducted for the closed system with the stopper permanently attached to the mass. This gave parameter values of $m^* = 0.058\,\text{g}$, $k^* = 464.49\,\text{N m}^{-1}$ and $c^* = 0.09235\,\text{N s m}^{-1}$. Figure 5 shows the experimentally derived frequency response compared with the optimized system parameters for the open 1-DOF system. The two curves show the optimized system agrees with the experimental results, particularly near the resonant operating point.

With the system parameters identified, these values can now be used to computationally model the PWL harvester. Inputting the extracted parameters into the computational tool, the maximum response envelope and the resonant gap sizes over the predetermined frequency range can be constructed and are shown in figure 6. Results from the Experimental study section are also plotted with the response envelope as well as a curve denoting the expected performance of the device at 90% of the computed resonant gap size.

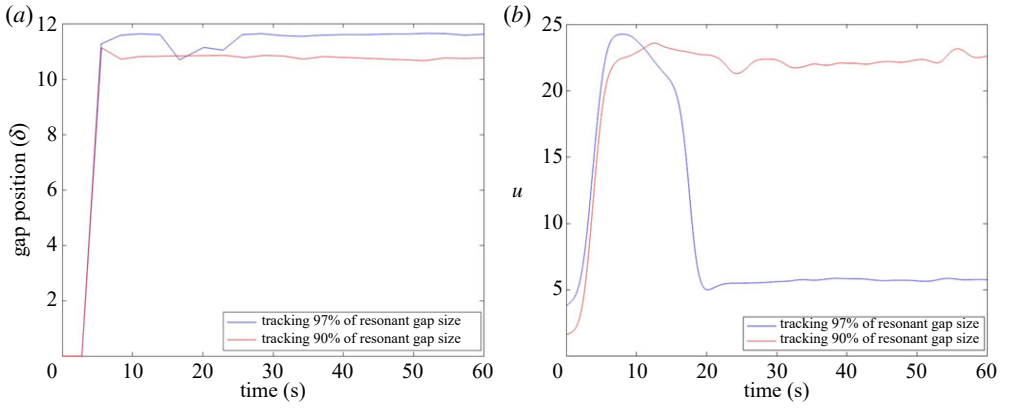

Figure 7. (*a*) Gap time history. (*b*) Displacement transmissibility time history.

4. Experimental study

In this section, the physical system with the control process is tested under varying excitation conditions. First, an example of the undesired jump phenomenon is given and the mitigation strategy is shown. Next, an example demonstrating how the gap control method is necessary to maximize the system response is given. The system is then excited by a frequency sweep where the active gap control is compared with fixed gap cases. Lastly, the power generation of the system is investigated.

(a) Jump phenomenon

One particular nonlinear dynamic property that has been observed by researchers of PWL systems is the jump phenomenon. This can occur when the response of the system jumps from the higher amplitude nonlinear response to the lower amplitude linear response. In this system, the jump phenomenon leads to the loss of intermittent contact between the oscillating mass and the mechanical stopper, causing a reduction in vibration amplitude. The previous computational study found that this phenomenon is more likely to occur when the gap size is very close to the computed resonant gap size, and by reducing the actual gap size, the system is more likely to preserve the intermittent contact and higher amplitude response [34]. This does come with a trade-off though of reduced performance compared with the full computed resonant gap size.

To illustrate this phenomenon, two cases of differing gap sizes are tested first. In this test, the system is excited by a harmonic base excitation with a fixed frequency of 16.5 Hz. One case uses 97% of the computed resonant gap size as the actual gap size while the other uses 90% of the computed size in order to prevent the jump phenomenon. The gap size time history can be seen in figure 7*a* along with the non-dimensionalized response u in figure 7*b*.

It can be seen that the gap size fluctuates in both cases due to the slightly changing estimates of frequency and amplitude by the signal estimator. This is due to the low levels of noise present in the measurement data as well as the excitation signal. For the response in red where the gap size is set to 90% of the computed δ_r, the system maintains intermittent contact and preserves the nonlinear response over the full testing period. In comparison, the case using 97% of the resonant gap size is shown to begin to increase in amplitude, but then jump to the linear response due to slight perturbations, significantly reducing vibration performance. This illustrates the trade-off between maximum performance and the possibility of experiencing the undesired jump phenomenon. To compare with expected performance, the steady-state displacement transmissibility of this test case is plotted with the maximum response envelope in figure 6 along with a number of additional experimental data points.

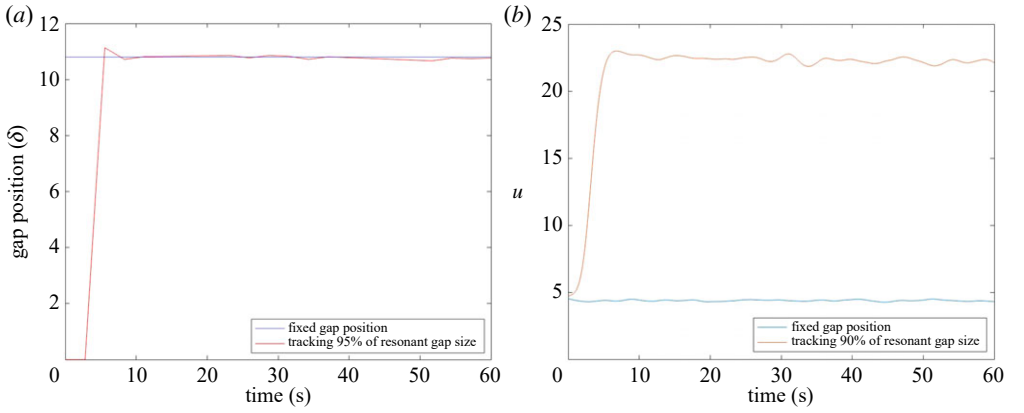

Figure 8. (*a*) Gap time history. (*b*) Displacement transmissibility time history.

(b) Gap control comparison

The reason this design shows increased performance compared with other harvesters using stoppers and gaps is due to the ability to control the gap. When the system is excited, it is necessary to gradually move the gap to the optimal position. This allows the harvester to accumulate energy and preserve the intermittent contact during the transient response. Figure 8 compares the performance of the harvester with a fixed gap size and with a gradual adjustment process. This process was conducted in two separate tests excited at 17.5 Hz. In the first, the gap is set to the precomputed optimal position before excitation. In the second test, the gap is set to the no gap position and then increased after the excitation begins.

As shown, this allows for the oscillator to gain energy and maintain the intermittent contact as the gap is increased to the optimal level. With the gap adjustment process, the oscillator is able to reach an amplitude of 22.29 when operating in the nonlinear response, whereas without the gap adjustment process, the average amplification is much lower at 4.38 since the oscillator remains in its linear state and never makes contact with the stopper. Since the intermittent contact is not maintained, the difference in performance also illustrates the improvement of the system over a simple linear harvester. The vibration amplification is increased by 5.09 times by adjusting the gap to ensure intermittent contact. It is shown that the gap adjustability and control process are necessary to ensure maximum performance, even for stationary excitation. The steady-state displacement transmissibility is plotted in figure 6 along with the maximum response envelope. Also plotted in figure 6 are other test points varying from 18.5 to 21.5 Hz. As shown, these points roughly follow the 90% response envelope and are all within 2.6% of the 90% optimal gap size line computationally predicted, and show the effectiveness of the modified computational approach presented herein in predicting the actual system response.

(c) Drifting excitation

Next, the system is excited by a drifting frequency excitation from 16 to 21 Hz. Note that in this test, 90% of the resonant gap size was again used as the chosen gap size to preserve intermittent contact for the gap control case. Two other cases with fixed gap sizes of $\delta = 0$ and 3.75 are also compared with the gap control case. The system responses and gap time histories are shown in figure 9.

Figure 9 shows that when tracking the optimal gap size, the PWL oscillator is able to maintain a large response amplitude and intermittent contact over the frequency sweep. In comparison, the fixed gap cases only showed good performance near the resonance peak and reduced performance elsewhere. It was observed that the case where the gap was fixed at $\delta = 3.75$ showed

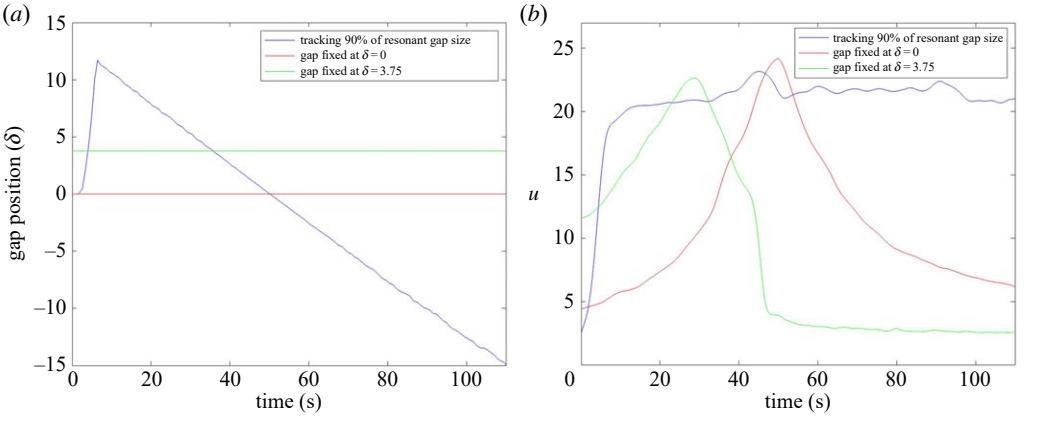

Figure 9. (*a*) Gap time history. (*b*) Displacement transmissibility time history.

greater bandwidth than the 0 gap case, though the system quickly jumped to the linear response after the peak. It can also be seen in the plots that the fixed gap cases show increased amplification at their respective peaks compared with the adjustable gap case. The difference in peaks for the $\delta = 3.75$ case can be attributed to the reduction in target gap size from the computational prediction. The no gap case also showed the same behaviour, peaking over the response of the active gap control case. The gap reduction should have no effect here due to the fact that the predicted gap size is 0. This discrepancy is indicative of a few things including error present in the resonant gap size predictions due to uncertainty in the frequency and amplitude estimation. Additionally, assumptions in the model of linear spring rate and a simple viscous damping model can contribute to this difference. Finally, delays in the estimator using previous response windows can also contribute to this discrepancy.

While the measured response in the active gap control case varied slightly from expected, overall the desired large amplitude response was maintained over the frequency sweep. In both figures 9 and 6, it is shown that the displacement transmissibility of the mass fluctuates slightly through the sweep between values of around 21–23 when values between 22 and 22.5 were expected. Comparing the three test cases, the no gap case showed an average amplification of 11.08 from the base vibration, the $\delta = 3.75$ case showed an average amplification of 8.65 and the active control method was able to reach an amplification of 21.42.

(d) Energy harvesting investigation

In this section, results from the energy generation part of the experiment are compared with the computational model. The transducer added to the system consists of a magnet added to the carriage with its poles aligned with the rail and a conductor coil wound around the mass's axis of motion. A model of the transducer used in this work is shown in the system model in figure 1.

The mechanical system causes relative motion between the magnet and coil that is amplified by the gap control system. This relative motion causes a flux variation in the coil turns, which in turn generates an induced emf. This coil was placed in parallel with a load resistor, where the induced voltage is measured. The parameters of the added transducer are given in table 2.

For the first test, the system was excited at 17.5 Hz and the active gap control method was used to maximize system performance. Figure 10 shows the amplified displacement as well as the instantaneous induced voltage. Note that 90% of the computed resonant gap size was used for this test case.

The measured system dynamics showed an RMS amplification with respect to the base motion of 15.03 once steady-state operation was reached. Compared with the expected result of 15.94, this gives an error of 6.07%. This error can again be attributed to the simple viscous

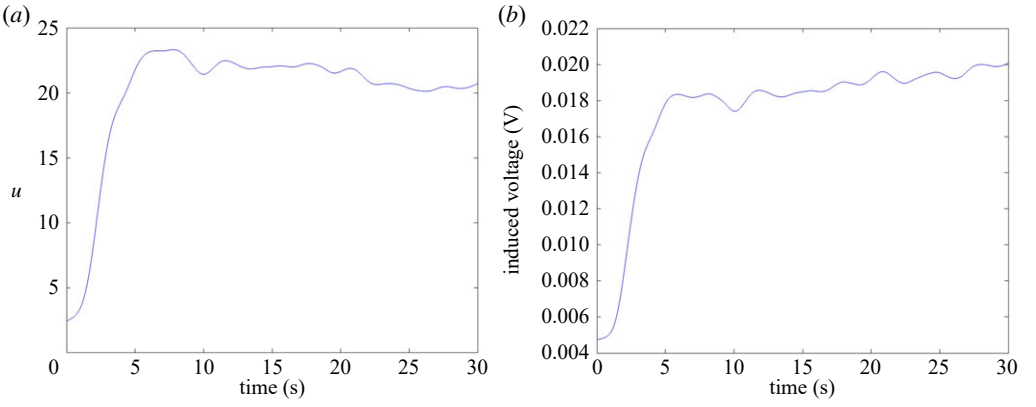

Figure 10. (*a*) Displacement transmissibility time history. (*b*) Induced voltage time history.

Table 2. Transducer parameters.

coil diameter (m)	0.0621	load resistance (Ω)	220
flux density (G)	14 800	coil length (m)	0.0429
no, coil turns	200		

damping model and linear spring rate that was assumed in the model as well as the reduced gap position. Some of the present error can also be attributed to electromagnetic damping, which was neglected in this work since the study focused on the dynamics of the system. As for the power generation, the average power at steady state was calculated to be 0.548 µW. The electromagnetic induction model predicted 0.592 µW, showing a 7.43% error from expected. This error can likely be attributed to the simplified model of the magnetic field. The model used assumed that there would be no interference from other ferromagnetic conductors, which can influence the field. Though an attempt was made to minimize the amount of ferromagnetic material near the harvester, there were still components that could have had an impact on the field.

Next, a frequency sweep was conducted to illustrate the improvement of the active gap control method compared with fixed gap cases as well as a linear harvesting method. In this test, the system was excited from 16 to 18 Hz over a period of 100 s. The dynamics as well as induced current in the coil were monitored. Figure 11 shows the plotted measurements over the test duration.

Starting with the linear response, it is shown that operating away from the 1 DOF system's resonant frequency leads to greatly reduced performance. For this case, an average power of 0.095 µW was calculated, by far the lowest of the test cases. For the fixed gap position, it can be seen that the response begins to gain energy until experiencing the jump phenomenon and dropping into the linear response. The plot shows that the fixed gap case experiences higher amplification than the active gap control method due to the reduction in gap size from the predicted resonance value. An average power of 0.429 µW was calculated for the testing period. As for the active gap control method, after the stopper moves to the operating position, it is able to maintain a high amplification for the duration of the testing period. As in the previous section, the amplification is slightly reduced near the end of the test period. This can again be attributed to slight errors in the characterization leading to slightly inaccurate resonant gap position predictions. This test case had an average power generation of 0.578 µW, a 608% increase from the linear case and a 74% increase from the fixed gap position. The improvement over the fixed gap cases will vary greatly depending on the frequencies excited as this test swept only 2 Hz of the tuned range.

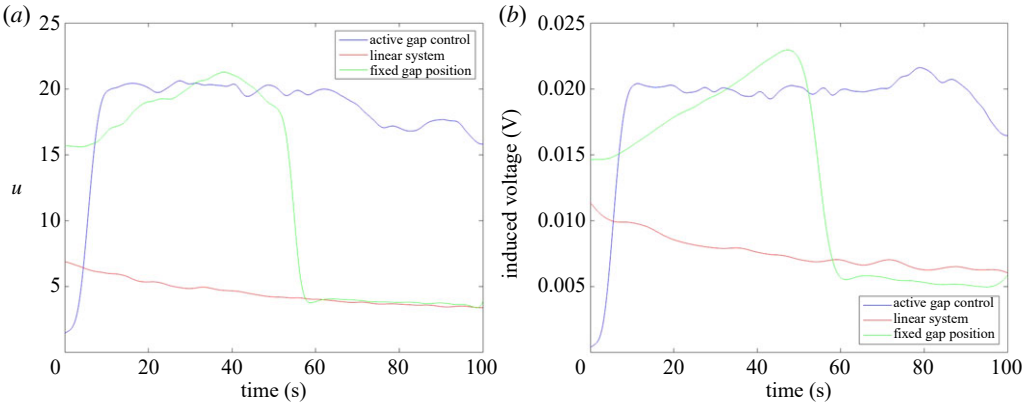

Figure 11. (*a*) Displacement transmissibility time history. (*b*) Induced voltage time history.

5. Conclusion and discussion

In this investigation, a PWL energy harvester with a controllable gap was studied for various excitation conditions both computationally and experimentally. To maximize the system performance, the resonant frequency was tuned to match the ambient vibrations by adjusting the gap position to the location precomputed by the BAA method. Also presented are modifications to the underlying computational work to better account for the physical system implementation, as well as a model of the energy harvesting method. The investigation showed that the measured system dynamics match the computational predictions reasonably well, although it was found in the frequency sweep case that the characterization of the system may require further refinement in future implementations. The investigation also showed that the model of the system's electrical generation did an adequate job of predicting the system's power generation, with some error present as expected due to simplifications in the model used.

In future work, further refinement of the system characterization should be completed. It was seen in the fixed frequency cases that the physical nonlinear system behaved as expected with measured displacement transmissibility following the predicted behaviour from the computational tool. The slight error between the experimental and computational performance can be attributed to errors in the characterization as well as assumptions of linear spring rate and a simple viscous damping model. While this test case did not show a need for a more effective characterization, the case of the frequency sweep did show some behaviour that deviated from expectations. Overall, the control system behaved as expected, maximizing the performance of the harvester by adjusting the gap position. The test case using the gap control method showed increased amplification compared with the fixed gap cases, and the displacement transmissibility predicted by the computational model was very close to what was present in the experiment. Future work could also include an investigation of the optimal a value used to scale down δ_r. In this work, a value was chosen to ensure intermittent contact for the test cases considered, but future work could include a study on harvested signal noise and perturbations in order to maximize this value for optimal performance.

As the focus of this investigation was the system dynamics and the implementation of the actively controlled gap, there was no analysis of the net power generated. Future studies of the proposed harvester should focus on optimizing the energy transducer to attain a fully self-powered system. In this investigation, the power used by the actuator, control process and sensors was not measured or compared with the power generated. In future implementations, low-power hardware should be leveraged to reduce the power necessary to operate the gap control system, ensuring there is a positive net-power gain. Another way to reduce required power is to remove one of the sensors used in the system. Currently, the control process assumes that the base

displacement is being measured and these data are used to determine the dominant frequency and amplitude. To reduce system complexity and power requirements, solely the PWL system response will be measured. The system response along with the known parameters can then be used to extract the dominant frequency and amplitude.

Lastly, future implementations of this design will be targeted to a specific application of energy harvesting, namely harvesting of ambient vibrations on rotating machinery. In the design process of this work, an arbitrary range of frequencies was chosen that would work for the bench-top testing. In subsequent iterations of the device, field measurements of rotating machinery in normal operating conditions will be conducted allowing for realistic design parameters. These future designs will also be implemented with a piezoelectric transducer as this method is increasingly common for similar systems and has a higher inherent energy density [46–48].

Data accessibility. This article has no additional data.

Declaration of AI use. We have not used AI-assisted technologies in creating this article.

Authors' contributions. J.V.: conceptualization, formal analysis, investigation, methodology, writing—original draft; K.D.: funding acquisition, project administration, resources, supervision, writing—review and editing.

Both authors gave final approval for publication and agreed to be held accountable for the work performed therein.

Conflict of interest declaration. We declare we have no competing interests.

Funding. This paper is based on work supported by the National Science Foundation (grant no. 1902408), program manager Dr Harry Dankowicz. Any opinions, findings and conclusions or recommendations expressed in this paper are those of the authors and do not necessarily reflect the views of the National Science Foundation.

Acknowledgements. The authors acknowledge Josh Gueth for his technical support in fabricating components for the experiment.

References

1. Prajwal KT, Manickavasagam K, Suresh R. 2022 A review on vibration energy harvesting technologies: analysis and technologies. *Eur. Phys. J. Spec. Top.* **231**, 1359–1371. (doi:10.1140/epjs/s11734-022-00490-0)
2. Mohanty A, Parida S, Behera RK, Roy T. 2019 Vibration energy harvesting: a review. *J. Adv. Dielect.* **9**, 1930001. (doi:10.1142/S2010135X19300019)
3. Khan FU, Iqbal M. 2016 Electromagnetic-based bridge energy harvester using traffic-induced bridge's vibrations and ambient wind. In *2016 Int. Conf. on Intelligent Systems Engineering* (*ICISE*), pp. 380–385. Islamabad, Pakistan: Hindawi. (doi:10.1109/INTELSE.2016.7475152)
4. Gunn B, Alevras P, Flint JA, Fu H, Rothberg SJ, Theodossiades S. 2021 A self-tuned rotational vibration energy harvester for self-powered wireless sensing in powertrains. *Appl. Energy* **302**, 117479. (doi:10.1016/j.apenergy.2021.117479)
5. Cooley CG, Chai T. 2017 Energy harvesting from the vibrations of rotating systems. *J. Vib. Acoust.* **140**, 021010. (doi:10.1115/1.4038106)
6. Nabavi SF, Farshidianfar A, Afsharfard A. 2018 Novel piezoelectric-based ocean wave energy harvesting from offshore buoys. *Appl. Ocean Res.* **76**, 174–183. (doi:10.1016/j.apor.2018.05.005)
7. Viet N, Xie X, Liew K, Banthia N, Wang Q. 2016 Energy harvesting from ocean waves by a floating energy harvester. *Energy* **112**, 1219–1226. (doi:10.1016/j.energy.2016.07.019)
8. Kilcher L, Fogarty M, Lawson M. 2021 Marine energy in the United States: an overview of opportunities. Technical report National Renewable Energy Lab (NREL) United States. (doi:10.2172/1766861)
9. Aderinto T, Li H. 2018 Ocean wave energy converters: status and challenges. *Energies* **11**, 1250. (doi:10.3390/en11051250)
10. Poulin G, Sarraute E, Costa F. 2004 Generation of electrical energy for portable devices. *Sensors Actuators A: Phys.* **116**, 461–471. (doi:10.1016/j.sna.2004.05.013)
11. Tran N, Ghayesh MH, Arjomandi M. 2018 Ambient vibration energy harvesters: a review on nonlinear techniques for performance enhancement. *Int. J. Eng. Sci.* **127**, 162–185. (doi:10.1016/j.ijengsci.2018.02.003)
12. Mann BP, Sims ND. 2009 Energy harvesting from the nonlinear oscillations of magnetic levitatio. *J. Sound Vib.* **319**, 515–530. (doi:10.1016/J.JSV.2008.06.011)

13. Quinn DD, Triplett AL, Bergman LA, Vakakis AF. 2010 Comparing linear and essentially nonlinear vibration-based energy harvesting. *J. Vib. Acoust.* **133**, 011001. (doi:10.1115/1.4002782)
14. Ramlan R, Brennan MJ, Mace BR, Kovacic I. 2010 Potential benefits of a non-linear stiffness in an energy harvesting device. *Nonlinear Dyn.* **59**, 545–558. (doi:10.1007/s11071-009-9561-5)
15. Van Blarigan L, Danzl P, Moehlis J. 2012 A broadband vibrational energy harvester. *Appl. Phys. Lett.* **100**, 253904. (doi:10.1063/1.4729875)
16. Harne RL, Wang KW. 2013 Prospects for nonlinear energy harvesting systems designed near the elastic stability limit when driven by colored noise. *J. Vib. Acoust.* **136**, 021009. (doi:10.1115/1.4026212)
17. Ghandchi Tehrani M, Elliott SJ. 2014 Extending the dynamic range of an energy harvester using nonlinear damping. *J. Sound Vib.* **333**, 623–629. (doi:10.1016/j.jsv.2013.09.035)
18. Vijayan K, Friswell MI, Haddad Khodaparast H, Adhikari S. 2015 Non-linear energy harvesting from coupled impacting beams. *Int. J. Mech. Sci.* **96–97**, 101–109. (doi:10.1016/j.ijmecsci.2015.03.001)
19. Liu JQ, Fang HB, Xu ZY, Mao XH, Shen XC, Chen D, Liao H, Cai BC. 2008 A MEMS-based piezoelectric power generator array for vibration energy harvesting. *Microelectron. J.* **39**, 802–806. (doi:10.1016/j.mejo.2007.12.017)
20. Marinkovic B, Koser H. 2012 Demonstration of wide bandwidth energy harvesting from vibrations. *Smart Mater. Struct.* **21**, 065006. (doi:10.1088/0964-1726/21/6/065006)
21. Wei C, Jing X. 2017 A comprehensive review on vibration energy harvesting: modelling and realization. *Renewable Sustainable Energy Rev.* **74**, 1–18. (doi:10.1016/j.rser.2017.01.073)
22. Wang W, Zhang Y, Wei ZH, Cao J. 2022 Design and numerical investigation of an ultra-wide bandwidth rolling magnet bistable electromagnetic harvester. *Energy* **261**, 125311. (doi:10.1016/j.energy.2022.125311)
23. Wang W, Li B, Liu S, Wei ZH. 2023 Bifurcation analysis and nonlinear dynamics of a rolling magnet multistable electromagnetic energy harvester. *Commun. Nonlinear Sci. Numer. Simul.* **118**, 107027. (doi:10.1016/j.cnsns.2022.107027)
24. Bendame M, Abdel-Rahman E, Soliman M. 2016 Wideband, low-frequency springless vibration energy harvesters: Part II. *J. Micromech. Microeng.* **26**, 115022. (doi:10.1088/0960-1317/26/11/115022)
25. Bendame M, Abdel-Rahman E, Soliman M. 2016 Wideband, low-frequency springless vibration energy harvesters: Part I. *J. Micromech. Microeng.* **26**, 115021. (doi:10.1088/0960-1317/26/11/115021)
26. Wang W, Wei H, Wei ZH. 2021 Numerical analysis of a magnetic-spring-based piecewise nonlinear electromagnetic energy harvester. *Eur. Phys. J. Plus* **137**, 56. (doi:10.1140/epjp/s13360-021-02255-5)
27. Liu H, Lee C, Kobayashi T, Tay CJ, Quan C. 2012 Investigation of a MEMS piezoelectric energy harvester system with a frequency-widened-bandwidth mechanism introduced by mechanical stoppers. *Smart Mater. Struct.* **21**, 035005. (doi:10.1088/0964-1726/21/3/035005)
28. Wu Y, Badel A, Formosa F, Liu W, Agbossou A. 2014 Nonlinear vibration energy harvesting device integrating mechanical stoppers used as synchronous mechanical switches. *J. Intell. Mater. Syst. Struct.* **25**, 1658–1663. (doi:10.1177/1045389X14533437)
29. Liu S, Cheng Q, Zhao D, Feng L. 2016 Theoretical modeling and analysis of two-degree-of-freedom piezoelectric energy harvester with stopper. *Sens. Actuators, A* **245**, 97–105. (doi:10.1016/j.sna.2016.04.060)
30. Abedini A, Wang F. 2019 Energy harvesting of a frequency up-conversion piezoelectric harvester with controlled impact. *Eur. Phys. J. Spec. Topics* **228**, 1459–1474. (doi:10.1140/epjst/e2019-800211-8)
31. Hoffmann D, Folkmer B, Manoli Y. 2009 Fabrication, characterization and modelling of electrostatic micro-generators. *J. Micromech. Microeng.* **19**, 094001. (doi:10.1088/0960-1317/19/9/094001)
32. Blystad LCJ, Halvorsen E. 2011 A piezoelectric energy harvester with a mechanical end stop on. *Microsyst. Technol.* **17**, 505–511. (doi:10.1007/S00542-010-1163-0)
33. Le CP, Halvorsen E, Søråsen O, Yeatman EM. 2012 Microscale electrostatic energy harvester using internal impacts. *J. Intell. Mater. Syst. Struct.* **23**, 1409–1421. (doi:10.1177/1045389X12436739)
34. Tien MH, D'Souza K. 2020 Method for controlling vibration by exploiting piecewise-linear nonlinearity in energy harvesters. *Proc. R. Soc. A* **476**, 20190491. (doi:10.1098/rspa.2019.0491)

35. Tien MH, D'Souza K. 2017 A generalized bilinear amplitude and frequency approximation for piecewise-linear nonlinear systems with gaps or prestress. *Nonlinear Dyn.* **88**, 2403–2416. (doi:10.1007/s11071-017-3385-5)
36. Tien MH, Hu T, D'Souza K. 2018 Generalized bilinear amplitude approximation and X-Xr for modeling cyclically symmetric structures with cracks. *J. Vib. Acoust.* **140**, 041012. (doi:10.1115/1.4039296)
37. Tien MH, Hu T, D'Souza K. 2019 Statistical analysis of the nonlinear response of bladed disks with mistuning and cracks. *AIAA J.* **57**, 4966–4977. (doi:10.2514/1.J058190)
38. Noguchi K, Saito A, Tien MH, D'Souza K. 2021 Bilinear systems with initial gaps involving inelastic collision: forced response experiments and simulations. *J. Vib. Acoust.* **144**, 021001. (doi:10.1115/1.4051493)
39. Tien MH, D'Souza K, Lu M. 2022 Efficient analysis of piecewise-linear nonlinear systems modeled using general state-space representations. *J. Comput. Nonlinear Dyn.* **17**, 081001. (doi:10.1115/1.4054152)
40. MATLAB. 2021 *Version 9.10.0 (R2021a)*. Natick, MA: The MathWorks.
41. Zhivomirov H, Nedelchev I, Vasilev R. 2016 A method for single-tone frequency estimation. *Rom. J. Vib. Acoust.* **13**, 20–24.
42. Lyons R. 2011 Reducing FFT scalloping loss errors without multiplication [DSP tips and tricks]. *IEEE Signal Process Mag.* **28**, 112–116. (doi:10.1109/MSP.2010.939845)
43. Tang X, Zuo L. 2009 Towards meso and macro scale energy harvesting of vibration. In *Proceedings of the ASME 2009 International Mechanical Engineering Congress and Exposition, Volume 10: Mechanical Systems and Control, Parts A and B, Lake Buena Vista, FL, 13–19 November*. ASME. (doi:10.1115/IMECE2009-10902)
44. Zuo L, Tang X. 2013 Large-scale vibration energy harvesting. *J. Intell. Mater. Syst. Struct.* **24**, 1405–1430. (doi:10.1177/1045389X13486707)
45. Chow T. 2006 *Introduction to electromagnetic theory: a modern perspective*. Burlington, MA: Jones and Bartlett Publishers.
46. Khazaee M, Rezaniakolaie A, Moosavian A, Rosendahl L. 2019 A novel method for autonomous remote condition monitoring of rotating machines using piezoelectric energy harvesting approach. *Sens. Actuators A: Phys.* **295**, 37–50. (doi:10.1016/j.sna.2019.05.016)
47. Tang X, Wang X, Cattley R, Gu F, Ball AD. 2018 Energy harvesting technologies for achieving self-powered wireless sensor networks in machine condition monitoring: a review. *Sensors* **18**, 4113. (doi:10.3390/s18124113)
48. Qi L, Pan H, Pan Y, Luo D, Yan J, Zhang Z. 2022 A review of vibration energy harvesting in rail transportation field. *iScience* **25**, 103849. (doi:10.1016/j.isci.2022.103849)